OPEN

NPG Asia Materials (2017) 9, e450; doi:10.1038/am.2017.202
www.nature.com/am

ORIGINAL ARTICLE

# Carbon-decorated iron oxide hollow granules formed using a silk fibrous template: lithium-oxygen battery and wastewater treatment applications

Taek-Seung Kim[1,3], Gwang-Hee Lee[1,3], Seun Lee[1], Yoon-Sung Choi[2], Jae-Chan Kim[1], Hee Jo Song[1] and Dong-Wan Kim[1]

**Hierarchical nanoarchitecture and phase control of iron oxides are important approaches for achieving multi-functionality for various applications. Herein, rice-grain-shaped iron oxide hollow structures were synthesized via a hydrothermal process using a silk fibrous template, and the crystalline phases ($\alpha$-$Fe_2O_3$, $Fe_3O_4$) were controlled by annealing. These structures were applied in a lithium-oxygen battery cathode and as adsorbents for wastewater treatment. The porosity, hollow interior, surface area, surface chemical composition and efficient carbon matrix of the C/$Fe_3O_4$ hollow granules obtained by annealing under Ar atmosphere were favorable for enhancing the oxygen reduction and evolution kinetics when applied as an electrocatalyst for lithium-oxygen batteries, and also led to superior adsorption of organic pollutants (Rhodamine B) from an aqueous medium. The C/$Fe_3O_4$ hollow granules were uniformly distributed and confined in the 3D nanoarchitecture; this morphology can offer rapid ion transport with improved electronic and chemical kinetics as well as superior adsorption of organic pollutants.**
*NPG Asia Materials* (2017) **9,** e450; doi:10.1038/am.2017.202; published online 17 November 2017

## INTRODUCTION

Almost all iron oxides exist in the crystalline form as hydroxides and oxide hydroxides, which are common compounds widespread in nature. The properties of iron oxides depend on the conditions that influence the crystal polymorphs and the particle size. Iron oxides have been studied for their potential utility in a wide range of important applications such as in energy devices/storage, biomedical science, catalysis and environmental fields.[1–5]

The crystalline phases (for example, $\alpha$-$Fe_2O_3$, $\gamma$-$Fe_2O_3$, and $Fe_3O_4$) and oxidation state (for example, $Fe^{2+}$ and $Fe^{3+}$) of iron oxides can be suitably controlled to achieve desirable properties and adaptive functions. Hematite ($\alpha$-$Fe_2O_3$) and magnetite ($Fe_3O_4$) are the most widely utilized iron oxide polymorphs. In hematite, the oxygen ions are closed-packed in a hexagonal lattice and the $Fe^{3+}$ ions occupy two-thirds of the octahedral sites in the hexagonal unit.[6] Magnetite belongs to the spinel family of minerals. It is composed of iron ions in mixed valance states, and is different from the other phases of iron oxide. The oxygen ions are closed-packed in a cubic lattice and the iron ions ($Fe^{2+}$, $Fe^{3+}$) are located in the spaces, including the tetrahedral sites (only $Fe^{2+}$) and octahedral sites ($Fe^{2+}$, $Fe^{3+}$), between the oxygen ions.[7] Since the oxygen ion is much larger than the iron ions, the lattice structure of the iron oxides is controlled by the arrangement of the oxygen ions.

Some theoretical studies have shown that control of the exposed surface structure can bring about remarkable changes in the molar ratio of the redox couples because of differences in the atomic arrangement and electronic structures, leading to quite different electrocatalytic activity. Based on density functional theory analysis of magnetite, the (001) facets effectively improve the electrocatalytic performance by acting as active sites.[8] These facets can easily generate oxygen vacancies that play an important role as electrocatalysts in the oxygen evolution reaction (OER).

Furthermore, iron oxides are important regulators of pollutants such as heavy metals and organic pollutants. The adsorption ability of iron oxides has been exploited to remove contaminants such as arsenic, chromium, cadmium, lead and organic dyes from wastewater.[1,9–11] The magnetic property of magnetite has also been exploited in the removal of contaminants from processed water, where the adsorbent could be readily magnetically recovered.[1]

Among the ways to manifest reliably various functions of iron oxides, the biomimetic mineralization approach features precisely controllable, sustainable and low-cost and environmentally benign to access multi-functional materials with highly ordered structures in various applications.[1,12] Previously, according to Fei *et al.*,[13] the $\alpha$-$Fe_2O_3$ mesocrystals were fabricated via using silk fibrous template for the application to photocatalysts. This biomimetic mineralization

[1]School of Civil, Environmental and Architectural Engineering, Korea University, Seoul, South Korea and [2]Korean Minjok Leadership Academy, Gangwon-do, South Korea
[3]These authors contributed equally to this work.
Correspondence: Professor D-W Kim, School of Civil, Environmental and Architectural Engineering, Korea University, 145, Anam-dong, Seongbuk-gu, Seoul 136-713, South Korea.
E-mail: dwkim1@korea.ac.kr
Received 7 July 2017; revised 9 September 2017; accepted 2 October 2017

approach is developed tuneable size and morphologies by simply varying the concentration of the silk fibroin.

Additionally, unique hierarchical hollow structures show greater promise for enhanced properties in fields such as energy conversion/storage, and medicine and many others because of the tunability of properties via hierarchical pore and reduced aggregation, compared to their bulk counterparts.[14–17] Large internal voids and doubled surface areas formed by well-ordered subunits of hollow structures could show enhanced performance of Li-$O_2$ batteries and water treatment.[18]

Herein, we present the design of rice-grain-shaped hollow structures by using a silk fibrous template. More importantly, this strategy is extended to develop a composite with hollow granules (HGs) consisting of $Fe_3O_4$ and carbon derived from the carbonized silk fibrous template in order to take advantage of the highly aligned nano/micro-structures with hierarchical pores and hollows to achieve multi-functionality. Particularly, the hollow structures can offer rapid ion transport with improved electronic and chemical kinetics.[19–21] Through ripening (or hollowing) and reduction processes, the prepared iron oxide HGs are modified to offer important merits: (i) high specific surface area for available active sites; (ii) hierarchical porosity for short diffusion pathways; (iii) control of $Fe^{2+}/Fe^{3+}$ redox system for high electrocatalytic activity; and (iv) defective carbon formation for removal of organic pollutants. To demonstrate the above merits, we applied the C/$Fe_3O_4$ HGs and $Fe_2O_3$ HGs in the Li-$O_2$ battery cathode and the adsorbent of pollutants.

## MATERIALS AND METHODS

### Preparation of silk fibroin solution

A silk fibroin solution was prepared according to a procedure previously reported by Cheng *et al.*[22] First, *Bombyx mori* cocoon silk was placed into a 0.02 M sodium bicarbonate ($NaHCO_3$, 99%, High Purity Chemicals, Sacado, Japan) solution that was boiled twice at 90 °C for 0.5 h. The cocoon silk was rinsed with distilled water several times. The extracted silk fibroin was dissolved in a 9.3 M lithium bromide (LiBr, 99%, Sigma-Aldrich, Darmstadt, Germany) aqueous solution by heating at 60 °C for 4 h. The solution was then dialyzed against distilled water using a dialysis tubular membrane (Cellu Sep T2, 6000–8000 MWCO, TX, USA) over the course of 72 h. The solution was centrifuged twice at 10 000 r.p.m. for 10 min at 4 °C. The final concentration of the silk solution was about 6%, as calculated by weighing the remaining solid after drying.

### Synthesis of iron oxide hollow granules

Iron(III) chloride ($FeCl_3$, 97%, Sigma-Aldrich, Darmstadt, Germany) was added to 75 ml of 0.5 wt% silk solution until the final Fe(III) concentration reached 0.08 mol $l^{-1}$ and the mixture was stirred for 0.5 h. The solution was sealed in a 100 ml Teflon-lined stainless steel autoclave and then heated at 180 °C for 12 h. The autoclave was cooled at room temperature; the product was then washed thrice with deionized water by centrifugation. Finally, the obtained powder was prepared by freeze drying below −50 °C for 12 h. This procedure was previously reported by Fei *et al.*[13] The as-prepared powder (silk fibroin/$Fe_2O_3$ hollow granules; sf-$Fe_2O_3$ HGs) was thermally treated for 3 h at 500 °C under air or Ar (100 sccm). After the thermal treatment, reddish-brown $Fe_2O_3$ HGs, and black C/$Fe_3O_4$ HGs were respectively obtained.

### Characterization of iron oxide hollow granules

All samples were characterized by field emission scanning electron microscopy (FE-SEM; Quanta 250 FEG, Hitachi, Japan), transmission electron microscopy and energy dispersive X-ray spectroscopy (TEM and EDS; JEM-2100F, JEOL, USA), X-ray diffraction (XRD; Smartlab, Rigaku, Japan), thermogravimetric analysis (TGA, STA 409 PC and QMS 403 C, NETZSCH, Germany), Brunauer-Emmett-Teller (BET; BELSORP mini II, BEL, Japan) analysis, X-ray photoelectron spectroscopy (XPS; PHI X-tool, ULVAC-PHI, Japan), Raman and Fourier Transform Infrared spectrometry (Raman and FT-IR; LabRam ARAMIS IR2, HORIBA JOBIN YVON, Japan), superconducting quantum interference device (SQUID; MPMS-7, Quandum Design), and particle size distribution and zeta potential analyzer (ELSZ-1000, Photal Otsuka Electronics, Japan).

### Electrochemical evaluation of Li-$O_2$ battery

Electrochemical analysis of the C/$Fe_3O_4$ HGs and the $Fe_2O_3$ HGs was performed using Swagelok-type cells. The electrode was prepared by mixing each of the obtained powders (45%) with Super P carbon black (45%) and carboxymethyl cellulose (10%; CMC, Aldrich, Average $M_w$ ~700,000, Darmstadt, Germany). The obtained slurry was spread onto nickel foam, and the loading weight of the electrode was adjusted to approximately 0.2 mg. The Li-$O_2$ cells were assembled in an Ar-filled glove box. The cells consisted of a lithium foil as the anode, a glass microfiber filter (Celgard 2400, Wellcos, Gunpo, Korea) as the separator, 1 m $LiNO_3$ (Alfa Aesar, anhydrous, ⩾99.999%) in *N,N*-dimethylacetamide (DMAc; Alfa Aesar, anhydrous, ⩾99.8%) as the electrolyte, the electrode and carbon cloth (W0S1002, CeTech, Taichung, Taiwan) as a gas diffusion layer. All measurements were conducted under 1.5 atm dry oxygen to avoid any negative effects of humidity and $CO_2$. The assembled cells were tested with an automatic battery cycler (WBCS 3000, WonATech, Seoul, Korea) in the voltage window of 2.0–4.5 V.

### Analysis of adsorption capacity of iron oxide hollow granules

The adsorption test was performed by the following procedure: the iron oxide samples (sf-$Fe_2O_3$ HGs, C/$Fe_3O_4$ HGs, $Fe_2O_3$ HGs) were respectively added to 15 ml of Rhodamine B (Rh. B) solution and sonicated for 1.5 min. Each solution was sealed and shaken (200 r.p.m.) for 2 h at 25 °C. Two hours later, the absorbents were eliminated from the solution by centrifugation or magnetic separation. The concentration of the solutions was then determined by using a UV-Vis spectrophotometer (S-3100, SCINCO, Seoul, Korea) to measure the intensity of absorption at 554 nm ($\lambda_{max}$).

## RESULTS AND DISCUSSION

### Formation mechanism and structural characterization of iron oxide hollow granules

The rice-grain-shaped hollow structures adopted two crystal phases of α-$Fe_2O_3$, namely, (hematite) and $Fe_3O_4$ (magnetite). The schematic illustration in Figure 1 summarizes the process for fabrication of the iron oxide-based HGs. The entire synthesis process proceeds via the following three steps: (i) extraction of silk fibroin from *B. mori* cocoon silk; (ii) growth of sf-$Fe_2O_3$ HGs by hydrothermal reaction of the precursors with the use of a silk fibrous template; (iii) phase transformation of the as-formed pristine sf-$Fe_2O_3$ HGs into $Fe_2O_3$ HGs or C/$Fe_3O_4$ HGs by annealing under different atmospheres. The $Fe_2O_3$ HGs was obtained by annealing at 500 °C under air atmosphere. This air-annealing can remove the silk fibrous through oxidation of organic matters. The C/$Fe_3O_4$ HGs was obtained by annealing at 500 °C under Ar atmosphere. This Ar-annealing can format carbon matrix through reduction of organic matters, and transform to $Fe^{2+}$ from some $Fe^{3+}$, resulting in phase transformation to magnetite from hematite.

In the first step, a *B. mori* cocoon silk fibroin solution was prepared by dissolving degummed natural cocoons in a 9.3 M LiBr solution (Figures 1a and b). The sf-$Fe_2O_3$ HGs originated from the special arrangement of the *B. mori* cocoon silk fibroin. The silk fibroin is composed of nano-β-crystallites that are connected by hydrophobic interactions among the polypeptide chains of the silk fibroin.[23,24] Generally, it is believed that hydrophobic/hydrophilic block copolymer structures may be assembled into β-crystallites via the nanofibrillar cross-linked network of the silk fibroin in solution (Figure 1c).[24–27] Analysis of the particle size distribution and zeta potential showed that the silk fibroin in the solution underwent aggregation when the temperature of the solution increased (Figure 1d). This behavior

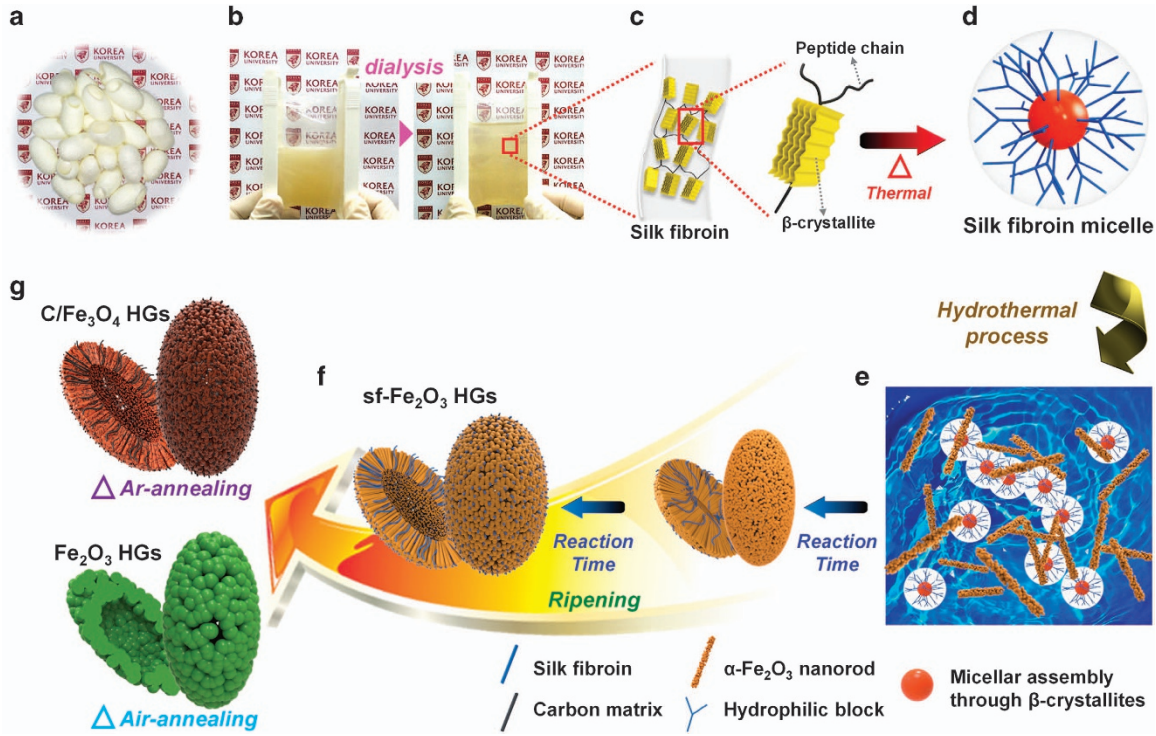


**Figure 1** Schematic illustration of preparation of iron oxide hollow granules. (**a**) Natural *B. mori* cocoons. (**b**) Dialysis of *B. mori* cocoon silk fibroin solution. (**c**) Model of *B. mori* cocoon silk fibroin. (**d**) Formation of silk fibroin micelle through heating. (**e**) In the early stage, $Fe_2O_3$ nanorods and silk fibroin micelle under hydrothermal conditions. (**f**) Formation of the sf-$Fe_2O_3$ HGs through ripening process, depending on reaction time. (**g**) Formation of the C/$Fe_3O_4$ HGs and $Fe_2O_3$ HGs by annealing. HGs, hollow granules.

probably involves interaction with $Fe^{3+}$, and thus the silk fibroin acts as a template for crystallization.

The functional groups of the extracted silk fibroin led to a zeta potential of −0.26 mV at room temperature (Supplementary Figure S1a). Heating the solution seemed to induce rearrangement of the fibroin molecules into more regular arrays along with formation of aggregates. After heating at 80 °C, the extracted silk fibroin in solution displayed a negative zeta potential of −9.04 mV (Supplementary Figure S1b). At room temperature, five peaks were observed around 21.7 nm, 97.9 nm, 241.1 μm, and 65 μm in the particle size distribution profile of the silk fibroin (Supplementary Figure S1c). This particle size distribution of the silk assembly suggests the formation of irregularly sized aggregates (or micelles) due to polypeptide chain folding and hydrophobic interactions.[24] However, after heating at 80 °C, the hydrodynamic diameters of the silk fibroin were concentrated at 95.8 nm and 370 nm. It is assumed that the hydrodynamic diameters of the silk fibroin prepared by heating affected the aggregation dynamics. The change of the hydrodynamic diameters provides evidence of crystallization at this stage in the process. The silk fibroin-induced formation of a nanofibrillar cross-linked network of the silk fibroin in the sf-$Fe_2O_3$ HGs. The results suggest that assembly and/or aggregation of the silk fibroin plays a significant role in the synthesis process.

In the second step, crystals of the sf-$Fe_2O_3$ HGs were fabricated by a hydrothermal process (Figures 1e–g). Apparently, in this experiment, it was the growth of hematite that led to the formation of the sf-$Fe_2O_3$ HGs through ripening process.[13,22] In the early stage, numerous α-$Fe_2O_3$ nanorods were formed via homogenous nucleation under hydrothermal conditions. The strong interaction between the $Fe^{3+}$ ions and hydrophobic nano-β-crystallite residues caused the silk fibroin to cover the numerous small crystallites, with growth of the crystal to minimize the surface energy (Figure 1e). Subsequently, a void space was formed inside of the primary $Fe_2O_3$ sphere structures by interaction of the hydrophobic/hydrophilic micelles. Eventually, a hollow space appeared in the interior of the sf-$Fe_2O_3$ HGs, as indicated by the schematic illustration (Figures 1e and f).

To further confirm the mechanism of formation of the sf-$Fe_2O_3$ HGs, time-dependent experiments were performed by using typical TEM and FE-SEM. After a short reaction time of 30 min (Supplementary Figures S2a and b), nanorods with an irregular morphology were obtained. When the reaction time was prolonged to 2 h (Supplementary Figures S2c–f), relatively uniform rice-grain-shaped structures were observed to form an actiniform nanorod bundle. The rice-grain-shaped structures underwent a hollowing process, and the hollow interior began to emerge. This observation provides direct evidence that the formation of the sf-$Fe_2O_3$ HGs is related to ripening. With further extension of the reaction time to 12 h (Figure 2a), the sf-$Fe_2O_3$ HGs did not change much in terms of size but became more uniform in terms of the rice-grain-shaped hollow structures. We identified silk fibroin through TEM analysis (Supplementary Figure S3). There is the silk fibroin inside the sf/$Fe_3O_4$ HGs. The silk fibroin is formatted to be the irregular amorphous shell of $Fe_2O_3$ structures (Supplementary Figures S3b, d).

In the third step, phase transformation of the sf-$Fe_2O_3$ HGs by annealing under Ar or air atmosphere generated the C/$Fe_3O_4$ HGs and $Fe_2O_3$ HGs, respectively. After annealing under Ar atmosphere (Figure 2b), the observed morphology and the particle size of the C/$Fe_3O_4$ HGs did not change significantly. However, after annealing under air atmosphere (Figure 2c), the low-magnification FE-SEM

image of the $Fe_2O_3$ HGs revealed shrinkage of the rice-grain-shaped hollow structures, and a more detailed FE-SEM image of the $Fe_2O_3$ HGs showed that the grain size of the shell structure was larger, as shown in the inset of Figure 2c. Figure 2d shows the XRD patterns of the starting the sf-$Fe_2O_3$ HGs and the resultant $Fe_2O_3$ HGs and C/$Fe_3O_4$ HGs. The XRD patterns of the sf-$Fe_2O_3$ HGs and the $Fe_2O_3$ HGs could be uniquely indexed to α-$Fe_2O_3$ (hematite, PDF card No. 33-0664). After annealing under Ar atmosphere, the hematite phase was completely transformed to the $Fe_3O_4$ (magnetite, PDF Card No. 74-0748) phase, as shown in part (iii) of Figure 2d.

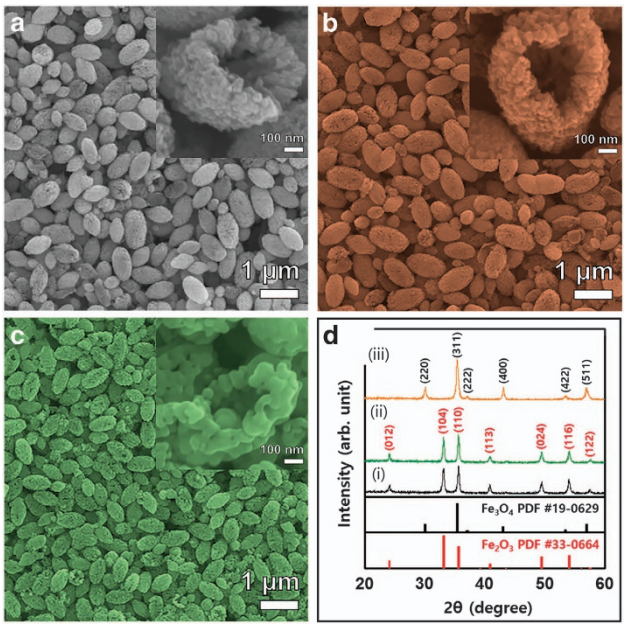


**Figure 2** Structure and morphology characterization of iron oxide hollow granules. Typical FE-SEM images of (**a**) sf-$Fe_2O_3$ HGs, (**b**) C/$Fe_3O_4$ HGs, and (**c**) $Fe_2O_3$ HGs, and (**d**) XRD patterns of (i) sf-$Fe_2O_3$ HGs, (ii) $Fe_2O_3$ HGs, and (iii) C/$Fe_3O_4$ HGs. HGs, hollow granules; XRD, X-ray diffraction.

The thermal behavior of the silk fibroin in the sf-$Fe_2O_3$ HGs was evaluated by TGA. As shown in Supplementary Figure S4a, the TGA curve of the sf-$Fe_2O_3$ HGs showed a 9.2% weight loss up to 400 °C, followed by a slow weight loss of 9.5% from 400 to 1000 °C, corresponding to loss of the polypeptide. The TGA curves of the $Fe_2O_3$ HGs showed a 1.1% weight loss up to 1000 °C, which indicates a pure crystal structure. The TGA curve of the C/$Fe_3O_4$ HGs showed a shoulder, followed by 1.7% weight gain around 300 °C. This behavior has also been observed for commercial $Fe_3O_4$ powders (50 nm, Alfa Aesar, 97%), apparently due to the oxidation of the $Fe^{2+}$ in magnetite. The weight percentage of carbon in the C/$Fe_3O_4$ HGs was determined to be 5.3% based on the difference between the TGA curves of the commercial $Fe_3O_4$ powder and that of the C/$Fe_3O_4$ HGs. We conducted additional analyses using TEM-EDS to obtain objective quantitative data (Supplementary Figure S5). The weight percentage of carbon of both C/$Fe_3O_4$ HGs and $Fe_2O_3$ HGs was observed to show a trend similar to that of TGA data. These results reveal that carbon species were generated through thermal decomposition of the silk fibroin. The C/$Fe_3O_4$ HGs were far superior to the $Fe_2O_3$ HGs in their ability to retain the morphology of the primary sf-$Fe_2O_3$ HGs, plausibly because loss of the carbon derived from the silk fibroin was low.

XPS and Raman spectroscopy (Supplementary Figures S4b and c) were used to estimate the carbon compositions of the samples. The C1s XPS spectrum of the C/$Fe_3O_4$ HGs clearly showed three peaks corresponding to carbon atoms in various functional groups and states, including $sp^2$ (C=C) bonded C at 283.7 eV and $sp^3$ (C–C) bonded species at 285.0 eV.[28] Generally, defects in the carbon structure can be distinguished from the ratio between the carbons

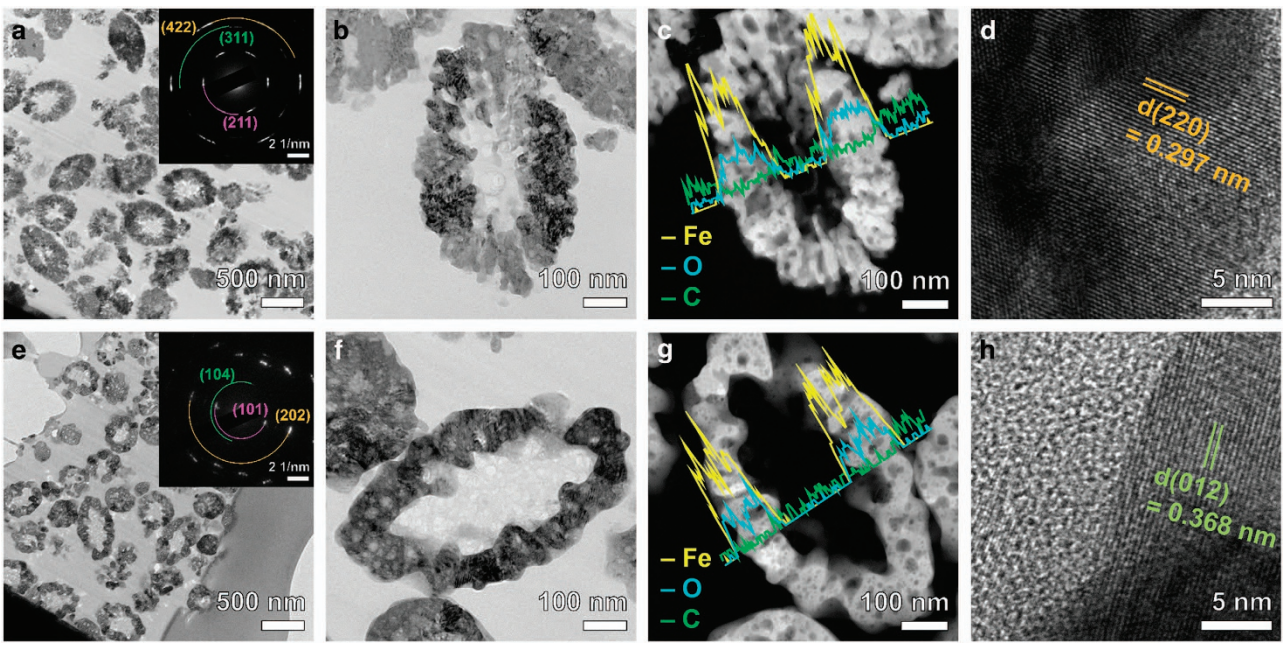


**Figure 3** Structural analysis of C/$Fe_3O_4$ HGs and $Fe_2O_3$ HGs. (**a**, **b**) Typical TEM, (**c**) HAADF STEM, and (**d**) HR-TEM images of cross-section of C/$Fe_3O_4$ HGs using FIB to obtain ultra-thin section. (**e**, **f**) Typical TEM, (**g**) HAADF STEM, and (**h**) HR-TEM images of cross-section of $Fe_2O_3$ HGs using FIB to obtain ultra-thin section. The insets of (**a**, **e**) are the corresponding SAED patterns and the HAADF STEM images in (**c**, **g**) include the EDS line-scan profiles. HGs, hollow granules; TEM, transmission electron microscopy; STEM, scanning transmission electron microscopy; HAADF, high-angle annular dark-field; HR-TEM, high-resolution TEM; FIB, focused ion beam; SAED, selected area electron diffraction; EDS, energy dispersive X-ray spectroscopy.

with $sp^3$ and $sp^2$ bonding. The ratio of $sp^3/sp^2$ bonded C in the $C/Fe_3O_4$ HGs was 0.9.[29] This result means that the $C/Fe_3O_4$ HGs had many defect sites. As shown in Supplementary Figure S4c, the Raman spectra were also analyzed in order to study the defect structure based on the D- and G-bands. The Raman spectra show two peaks at around 1320 and 1579 $cm^{-1}$, corresponding to the D- and G-bands of carbon, respectively. The value of the intensity ratio ($I_D/I_G$) was 1.50 for the $C/Fe_3O_4$ HGs. Both the $I_D/I_G$ ratio and the $sp^3/sp^2$ ratio exhibit to demonstrate the presence of defective carbon. The high intensity ratio of the D- and G-bands indicates a highly disordered carbon structure with increased $sp^3$ bonding. Therefore, the results from the Raman spectra agree well with the XPS analysis, indicating that the $C/Fe_3O_4$ HGs contained many defect sites.

We have confirmed by TEM that most of the carbon is present inside the $C/Fe_3O_4$ HGs. As shown in Supplementary Figure S6, there is a carbon matrix inside the $C/Fe_3O_4$ HGs. We identified carbon through EDS point analysis (Supplementary Figure S7). The carbon matrix is amorphous carbon, which is in good agreement with the results of XPS and Raman analysis (Supplementary Figure S4). On the surface of the outer $C/Fe_3O_4$ HGs, there is a thin and heterogeneous amorphous shell of about 1 nm (Supplementary Figure S6c). This amorphous shell is carbon derived from silk fibroin.

The variations in the phase and microstructure of the $C/Fe_3O_4$ HGs and the $Fe_2O_3$ HGs were investigated in further detail by acquiring TEM images and the corresponding selected area electron diffraction data. Focused ion beam analysis of the cross-sectional morphology of the $C/Fe_3O_4$ HGs and the $Fe_2O_3$ HGs was performed, as shown in Figure 3. The $C/Fe_3O_4$ HGs and the $Fe_2O_3$ HGs clearly maintained the hollow morphology, as indicated by the TEM image and the high-angle annular dark-field scanning TEM–energy-dispersive X-ray spectroscopic (HAADF STEM–EDS) data. The high-resolution TEM (HRTEM) image in Figure 3d shows that the inter-planar distance in the $C/Fe_3O_4$ HGs is 0.297 nm, which is consistent with the (220) plane of the magnetite phase. Figure 3h shows that the highly crystalline nature of hematite is preserved in the $Fe_2O_3$ HGs. The inter-planar distance of the $Fe_2O_3$ HGs is 0.368 nm, which corresponds to the (012) plane.

Although the rice-grain-shaped hollow structure was almost the same for both the $C/Fe_3O_4$ HGs and the $Fe_2O_3$ HGs after the annealing process, the porous architecture of the two samples, including the crystallite size and porosity, changed significantly (Supplementary Figure S8). Based on the aforementioned analysis, it can be expected that survival of the carbon matrix or the silk fibrous template would result in a highly porous shell structure after annealing. We believe that carbon matrix or silk fiber templates can maintain the porous shell structure and open channel structure and contribute to column grain growth, compared to the $Fe_2O_3$ HGs. After annealing under Ar atmosphere, the grain direction remains along the dashed line in Supplementary Figure S8a. However, in the $Fe_2O_3$ HGs (Supplementary Figure S8b), the silk fibroin was removed during air-annealing process, and then grain growth of the $Fe_2O_3$ HGs was generated randomly as indicated by the dashed circle.

The porosity of the sf-$Fe_2O_3$ HGs, the $C/Fe_3O_4$ HGs and the $Fe_2O_3$ HGs was investigated using $N_2$ adsorption-desorption analysis. Supplementary Figure S9 shows the $N_2$ adsorption–desorption isotherms and Barrett–Joyner–Halenda (BJH) pore size distribution curves for all the samples. The results are summarized in Supplementary Table S1. The BET specific surface areas of the sf-$Fe_2O_3$ HGs, the $C/Fe_3O_4$ HGs and the $Fe_2O_3$ HGs were determined to be 18.42, 35.83 and 10.16 $m^2 g^{-1}$, respectively; the pore volumes of these three samples were 0.05, 0.10 and 0.04 $cm^3 g^{-1}$, respectively. The pore size distribution decreased from 32 to 16 nm during annealing under Ar atmosphere. However, after annealing under air atmosphere, the pore size distribution was maintained at 32 nm (Supplementary Figures S9b, d, and f). The pore diameter peak at 4 nm disappeared after annealing in air atmosphere, whereas the peak at 4 nm was maintained after annealing in Ar atmosphere. Because the silk fibroin or carbon matrix can prevent grain growth, the $C/Fe_3O_4$ HGs maintained porous hollow and open-channel structures of the primary sf-$Fe_2O_3$ HGs, compared with the $Fe_2O_3$ HGs. These results are consistent with the HAADF STEM analysis (Supplementary Figure S8).

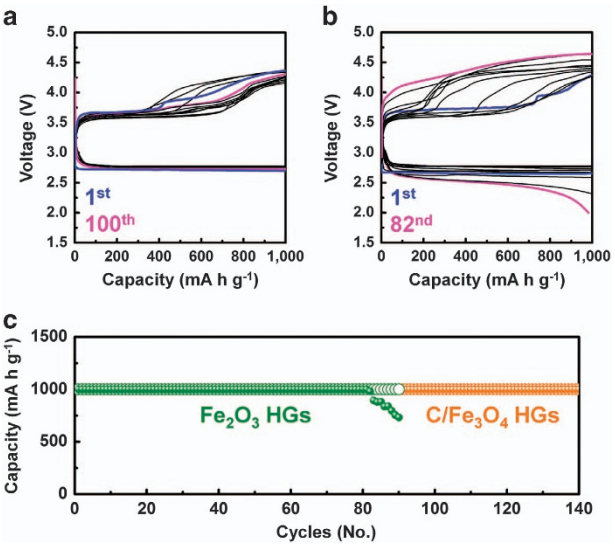


**Figure 4** Electrochemical characteristics of iron oxide hollow granules electrodes. Galvanostatic discharge–charge curves of (**a**) $C/Fe_3O_4$ HG and (**b**) $Fe_2O_3$ HG electrodes at a current density of 200 mA $g^{-1}$ under the fixed capacity regime of 1000 mA h $g^{-1}$. (**c**) Comparison of the discharge–charge specific capacity versus the cycle number of the $C/Fe_3O_4$ HG and $Fe_2O_3$ HG electrodes. HG, hollow granule.

**Use of iron oxide hollow granules as electrocatalyst in Li-$O_2$ battery**

To evaluate the electrocatalytic activity of iron(II,III) oxide and iron (III) oxide on the electrochemical performance of the Li-$O_2$ battery using the $C/Fe_3O_4$ HGs and the $Fe_2O_3$-containing air cathode ($C/Fe_3O_4$ HG electrode and $Fe_2O_3$ HG electrode), the galvanostatic discharge–charge cycles of a Li-$O_2$ cell with the $C/Fe_3O_4$ HG electrode were compared with those of a Li-$O_2$ cell employing the $Fe_2O_3$ HG electrode at a current density of 200 mA $g^{-1}$ and a fixed capacity regime of 1000 mA h $g^{-1}$, as shown in Figure 4. The overpotential of the $C/Fe_3O_4$ HG electrode was more stable than that of the $Fe_2O_3$ HG electrode during 100 discharge–charge cycles (Figures 4a and b). The galvanostatic discharge curves of the $C/Fe_3O_4$ HG electrode exhibited a minor change in the voltage ($< 0.1$ V) compared to that of the $Fe_2O_3$ HG electrode. The $Fe_2O_3$ HG electrode exhibited lower stability in the charge process during 82 cycles, compared with the $C/Fe_3O_4$ HG electrode (Figure 4b). The $Fe_2O_3$ HG electrode underwent sudden performance deterioration in the discharge process after the 80th cycle because of inefficient oxygen evolution kinetics. As shown in Figure 4c, the $C/Fe_3O_4$ HG electrode exhibited low overpotential (1.08 V at 140 cycle), which is one of the lowest overpotential, among previously reported all transition metal oxide electrocatalysts over long-term cycling (Supplementary Figure S10 and Supplementary Table S2). Structural defects and the surface oxidation state have been

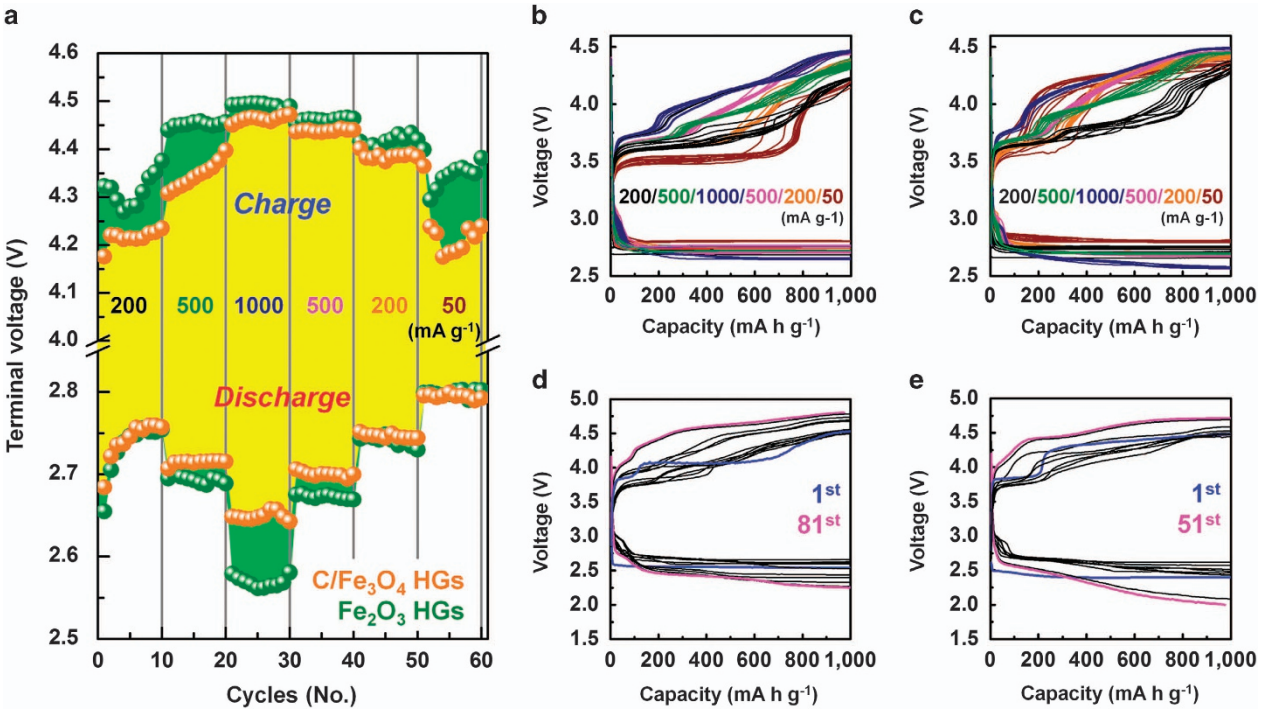


**Figure 5** Electrochemical performances of iron oxide hollow granules electrodes at various current densities. (**a**) Comparison of the discharge–charge terminal voltages versus the cycle number of the C/$Fe_3O_4$ HG and $Fe_2O_3$ HG electrodes at various current densities under the fixed capacity regime of 1000 mA h $g^{-1}$ and the corresponding galvanostatic discharge–charge curves of (**b**) C/$Fe_3O_4$ HG and (**c**) $Fe_2O_3$ HG electrodes. Galvanostatic discharge–charge curves of (**d**) C/$Fe_3O_4$ HG and (**e**) $Fe_2O_3$ HG electrodes at a current density of 1000 mA $g^{-1}$ under the fixed capacity regime of 1000 mA h $g^{-1}$.

suggested to have a major effect on the electrocatalytic activity of transition metal oxides in Li-$O_2$ batteries.[30–33] For example, density functional theory and experimental studies on manganese oxides for electrocatalyst application have shown that $MnO_2$ exhibits excellent oxygen reduction reaction and OER activity when more $Mn^{3+}$ ions are exposed on the surface than $Mn^{4+}$. In another case, $MnMoO_4$ exhibited higher catalytic activity when a higher content of vacancy defects was generated in the Mn-O-Mo framework sublattices.[31]

The difference in the surface oxidation state of the C/$Fe_3O_4$ HGs and the $Fe_2O_3$ HGs is significant, as indicated by the XPS data in Supplementary Figure S11. The Fe $2p_{3/2}$ spectra could be decomposed into two peaks at binding energies of 709.7 and 711.2 eV, corresponding to the $Fe^{2+}$ and $Fe^{3+}$ oxidation states, respectively. The Fe $2p_{3/2}$ peak for the C/$Fe_3O_4$ HGs was negatively shifted (to lower binding energy), indicating that the exposed surface Fe ions were more extensively reduced to $Fe^{3+}$ compared to those of the $Fe_2O_3$ HGs. The results presented in Supplementary Table S3 show that Fe in the C/$Fe_3O_4$ HGs is present in lower oxidation states, the $Fe^{2+}/Fe^{3+}$ molar ratio being approximately unity (that is, $Fe^{2+}/Fe^{3+} = 0.93$). However, the $Fe^{2+}/Fe^{3+}$ molar ratio in the surface layer of the $Fe_2O_3$ HGs decreased from 0.93 to 0.34.

The O 1s spectra presented two peaks at binding energies of 529.6 and 531.1 eV, representing the O 1s level in the C/$Fe_3O_4$ HGs (Supplementary Figure S11b), while the profile of the $Fe_2O_3$ HGs featured three peaks at binding energies of 529.4, 530.9 and 532.0 eV. The O 1s peak at higher binding energy (532.0 eV) is associated with chemisorbed or dissociated oxygen or OH species, such as adsorbed $H_2O$ or $O_2$ adsorbed on the surface of the materials.[34] In particular, absorption of water on the surface of the air cathode results in an undesirable effect in Li-$O_2$ batteries.[35] The content of oxygen vacancies in the C/$Fe_3O_4$ HGs was higher than that in the $Fe_2O_3$ HGs. From this observation, it can be concluded that the C/$Fe_3O_4$ HGs are more deficiently coordinated with oxygen during the annealing process under reducing atmosphere than in the case of the $Fe_2O_3$ HGs. Interestingly, we clearly show that the C/$Fe_3O_4$ HGs offer the opportunity to explore the effect of the oxidation states and oxygen vacancies on the oxygen reduction reaction and OER activity in Li-$O_2$ batteries.

In addition, structural defects present on the carbon are important factor for electrocatalytic activity in non-aqueous electrolyte systems. We demonstrated that disordered or defected carbon have more efficient oxygen reduction reaction (ORR) and OER activities than graphitic carbon.[29] Also, the carbon matrix of the C/$Fe_3O_4$ HGs is present in voids (pores between $Fe_3O_4$ nanostructures, hollow structure) of C/$Fe_3O_4$ HGs. The carbon matrix of the C/$Fe_3O_4$ HGs is less electrical conductive than graphitic carbon, but can improve the electrical conductivity of the C/$Fe_3O_4$ HGs. We believe that the carbon matrix can buffer the problems caused by insulating oxygen reduction reaction products such as $Li_2O_2$ present during discharge–charge cycles.

In order to further investigate the rate capability of the C/$Fe_3O_4$ HGs electrode, galvanostatic discharge–charge tests were also performed at current densities of 50, 200, 500 and 1000 mA $g^{-1}$ (Figures 5a–c). Figure 5a shows a comparison of the rate capabilities of the C/$Fe_3O_4$ HG and $Fe_2O_3$ HG electrodes. The overpotential of the C/$Fe_3O_4$ HG electrode was lower than that of the $Fe_2O_3$ HG electrode at initial current densities of 200, 500 and 1000 mA $g^{-1}$, respectively, which represents good recovery of the terminal voltages during discharge–charge cycling at 500 and 200 mA $g^{-1}$, respectively, after cycling at 1000 mA $g^{-1}$ under reverse conditions. After 50th discharge–charge cycling at various current densities, it was found that at the current density of 50 mA $g^{-1}$, the charge plateaus of the C/$Fe_3O_4$ HG electrode was reduced to 3.56 V, which is lower than that of the $Fe_2O_3$ HG electrode (4.29 V) (Figures 5b and c). The C/$Fe_3O_4$

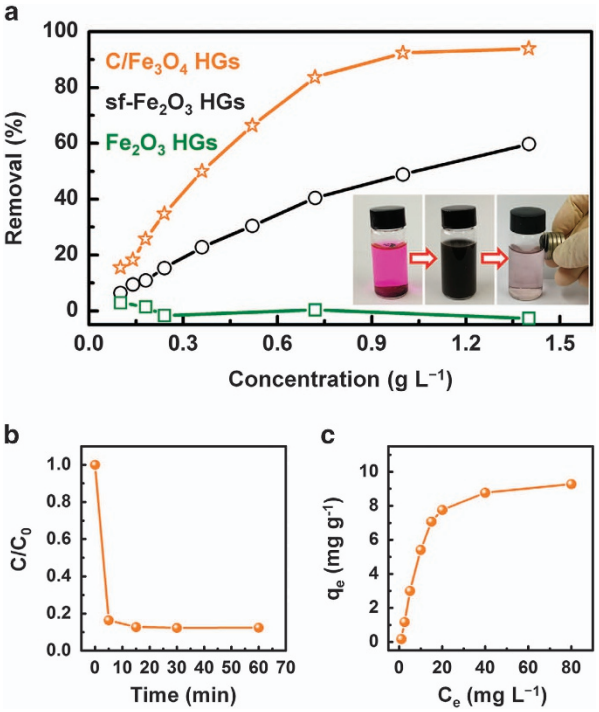


**Figure 6** Performance characteristics of adsorption process. (**a**) Removal efficiency of the sf-$Fe_2O_3$ HGs, C/$Fe_3O_4$ HGs and $Fe_2O_3$ HGs for adsorption of 5 mg $l^{-1}$ Rh. B with increasing amount of absorbent. (**b**) Rate of adsorptive removal of Rh. B (5 mg $l^{-1}$) by C/$Fe_3O_4$ HGs. The concentration of the C/$Fe_3O_4$ HGs was 1.4 g $l^{-1}$. (**c**) Adsorption isotherm for C/$Fe_3O_4$ HGs with increasing concentration of Rh. B. The concentration of C/$Fe_3O_4$ was 1.4 g $l^{-1}$ and the adsorption time was 2 h. HGs, hollow granules; Rh. B, Rhodamine B.

HG electrode revealed a remarkably low overpotential (0.76 V) compared with that of the $Fe_2O_3$ HG electrode (1.49 V) at specific capacity of 500 mA h $g^{-1}$ during 10 cycles (Supplementary Figure S12). In our previous report, the low overpotential reveals to contribute a strong OER activity, which generates actively $O_2$ gas, following that $Li_2O_2$ begin to quickly decompose.[31] Whereas high overpotential indicates that some $CO_2$ gas evolved at the end of the charge, corresponding to the decomposition of the carbon-containing electrolyte. The C/$Fe_3O_4$ HG electrode reveals for enhancing the OER activity. These results achieve by the C/$Fe_3O_4$ HGs with large specific surface area/pore volume and effective oxidation states/oxygen vacancies, compared with $Fe_2O_3$ HGs. To gain further insight, the performance of the C/$Fe_3O_4$ HG electrode in a Li-$O_2$ battery at high rate density was evaluated. Figures 5d and e show the galvanostatic discharge–charge cycling performance of the C/$Fe_3O_4$ HG and $Fe_2O_3$ HG electrodes in the fixed capacity regime of 1000 mA h $g^{-1}$ at a rate of 1000 mA $g^{-1}$. The $Fe_2O_3$ HG electrode exhibited a sudden deterioration of the discharge–charge overpotential at the 50th cycle (Figure 5e), and the super P electrode exhibited unstable discharge capacities after 27th cycle (Supplementary Figure S13). The C/$Fe_3O_4$ HG electrode exhibited more stable cycling performance over 80 cycles compared to the $Fe_2O_3$ HG electrode.

**Rhodamine B removal by adsorption on iron oxide hollow granules**

The effectiveness of the sf-$Fe_2O_3$ HGs, C/$Fe_3O_4$ HGs and $Fe_2O_3$ HGs for the adsorptive removal of Rh. B dye (used in the textile industry) was evaluated. Rh. B is a carcinogenic organic pollutant that is discharged into aqueous systems. Transitional water treatment techniques, including filtration, flocculation, membrane processes and advanced oxidation processes, are not good choices for removal of organic pollutants due to their low cost-effectiveness. The adsorption process is a more effective way to remove dyes than the other approaches. Iron oxides and carbon-based nanomaterials have frequently been reported to be effective for removal of organic pollutants.[1,36,37]

As observed in Figure 6a, the efficiency of removal of the dye by the sf-$Fe_2O_3$ HGs and C/$Fe_3O_4$ HGs was proportional to the concentration of the adsorbents. The C/$Fe_3O_4$ HGs exhibited the highest removal efficiency among the three samples. The removal efficiency of the C/$Fe_3O_4$ HGs increased from 15.4 to 94.0% when the amount of added absorbent was increased from 0.1 to 1.4 g $l^{-1}$. Furthermore, the C/$Fe_3O_4$ HGs can be easily separated from wastewater due to the magnetic property of magnetite. Magnetization curves were obtained by VSM at 300 K to confirm the magnetic property of $Fe_2O_3$ HGs and C/$Fe_3O_4$ HGs (Supplementary Figure S14). The $Fe_2O_3$ HGs have no magnetism, while the C/$Fe_3O_4$ HGs exhibit superparamagnetic property at 300 K. This diagram also shows the saturation magnetization of C/$Fe_3O_4$ HGs is 100.61 emu $g^{-1}$, which results that C/$Fe_3O_4$ HGs have the strong magnetism enough to be attracted by an external magnetic field in wastewater.

The removal efficiency of the sf-$Fe_2O_3$ HGs increased from 6.4 to 59.8% when the amount of absorbent added was increased from 0.1 to 1.4 g $l^{-1}$. The $Fe_2O_3$ HGs were inactive as an absorbent. As shown in Figure 6a and Supplementary Figure S15, the adsorption capacities of the samples for Rh. B followed the order: $Fe_2O_3$ HGs < sf-$Fe_2O_3$ HGs < C/$Fe_3O_4$ HGs, which is linked to the BET-specific surface area, where a higher surface area provides more active sites for adsorption. Moreover, because the C/$Fe_3O_4$ HGs include the carbon matrix derived from the silk fibrous template, they can efficiently remove Rh. B. Therefore, the C/$Fe_3O_4$ HGs exhibited the highest removal efficiency among the evaluated samples.

Investigation of the kinetics and adsorption isotherm of the C/$Fe_3O_4$ HGs was carried out as shown in Figures 6b and c. Figure 6b shows that the equilibrium adsorption time of Rh. B was reached to achieve fast within 15 min. The adsorption isotherm data (Figure 6c) show the relationship between the adsorption capacity (which is the amount of adsorbed adsorbate) and the equilibrium concentration of Rh. B in solution. To gain deeper insight from the kinetics and isotherm, the data were plotted in Supplementary Figures S16 and S17, respectively. The kinetics data for the C/$Fe_3O_4$ HGs (Supplementary Figure S16) fit more adequately to the pseudo-second-order model, having the highest correlation coefficient of 0.999. This suggests that the sorption mechanism is based on chemisorption and that the electrons are shared and exchanged between the pollutant and absorbent by valance forces.[38]

The adsorption isotherm data for the C/$Fe_3O_4$ HGs (Supplementary Figure S17) were more suitably fitted to the Langmuir equation than the Freundlich equation. This suggests that the adsorption process proceeded with monolayer coverage. The parameters for the kinetics and adsorption model and the correlation coefficient for the C/$Fe_3O_4$ HGs are summarized in Supplementary Table S4. The C/$Fe_3O_4$ HGs showed superior performance compared to commercial $Fe_3O_4$ powder and commercial $TiO_2$ (P25, Degussa). Compared with the commercial $Fe_3O_4$ powder (removal efficiency: 4.8%), the C/$Fe_3O_4$ HGs (removal efficiency: 96.4%) displayed extraordinarily high efficiency for removal of Rh. B (Supplementary Figure S18 and Table S5).

Compared with the previous literature, the adsorption capacity of the C/$Fe_3O_4$ HGs is lower than that of $BiFe_{0.95}Co_{0.05}O_3$, but the

C/$Fe_3O_4$ HGs exhibited excellent adsorption capacity in iron oxide/carbon composites (excluding graphene and CNT materials). The C/$Fe_3O_4$ HGs also exhibited relatively fast adsorption performance in transition metal oxides based adsorbents (Supplementary Table S6).

The large disparity between the performance of the C/$Fe_3O_4$ HGs and commercial $Fe_3O_4$ is caused by two main factors. The first is the hollow structure and mesoporous surface of the C/$Fe_3O_4$ HGs. These morphologies can offer a high surface area and active sites. We studied further to confirm the adsorption capacities of C/$Fe_3O_4$ HGs depending on width of hollow space. When the reaction time was prolonged to 2 h (provided in Supplementary Figures S2c − f), relatively uniform rice-grain-shaped structures were observed to form an actiniform nanorod bundle and to evolve hollow interior less. We transformed the less ripened sf-$Fe_2O_3$ HGs into the $Fe_3O_4$ phase by Ar-annealing (H2h-C/$Fe_3O_4$ HGs). When the Rh. B adsorption performance was evaluated, the narrow hollow interior of H2h-C/$Fe_3O_4$ HGs show poor adsorption performance. However, the largely hollow interior of the C/$Fe_3O_4$ HGs shows excellent adsorption performance (Supplementary Figure S19). We demonstrate that these results clearly shows the advantages of hollow structures.

The second reason is the presence of defect carbon in the composite, as indicated by XPS and Raman analysis. The defect carbon in the C/$Fe_3O_4$ HGs adsorbs Rh. B, having rich aromatic rings, through π–π stacking on the carbon matrix of the C/$Fe_3O_4$ HGs. The strength of π–π stacking is greatly dependent on the functional groups attached to the aromatic rings for organic chemicals.[39,40] In other words, the electrostatic and van der Waals interactions are the major contributions. We believe that the functional groups of carbon (such as –OH and –COOH) might have considerable effects on the adsorption of organic chemicals. Therefore, we additionally performed FT-IR analysis (Supplementary Figure S20). The FT-IR spectra of the C/$Fe_3O_4$ HGs show thee peaks, located at 2357, 1738 and 1365 $cm^{-a}$, which can be ascribed to the oscillation of carboxyl groups (–COOH). The presence of carboxyl groups as oxygen-containing functional groups in the C/$Fe_3O_4$ HGs is clearly evident by a C = O, C–H and O–H peaks. We measured the Rh. B adsorption performance of the carbon-removed $Fe_3O_4$ HGs (Supplementary Figure S21), comparing with that of the C/$Fe_3O_4$ HGs. As expected, the C-removed $Fe_3O_4$ HGs exhibit poorer adsorption performance (removal rate: 3.4%) than that of the C/$Fe_3O_4$ HGs (removal rate: 96.4%) (Supplementary Figure S18 and Supplementary Table S5). Therefore, the unique structure and defective carbon of the C/$Fe_3O_4$ HGs are effective for removal of organic pollutants for water treatment.

## CONCLUSION

The phase-controlled systematic synthesis of C/$Fe_3O_4$ HGs and $Fe_2O_3$ HGs was demonstrated, where the functionalities of the HGs were tailored for Li-$O_2$ battery and water treatment applications. The initial step for synthesizing the two controlled structures involves synthesis of the sf-$Fe_2O_3$ HGs by a hydrothermal process using the silk fibrous template, which provides a uniform size distribution of the rice-grain-shaped hollow structures to maximize their function. The silk fibrous template not only mediates effective attachment of the $Fe_2O_3$ crystalline structures but also serves as useful carbon after annealing under Ar atmosphere. This annealing process allows the fabrication of porous, hollow structures with large surface areas, consisting of a composite between carbon and magnetite, $Fe_3O_4$. The C/$Fe_3O_4$ HGs exhibit enhanced electrocatalytic activity and adsorption efficiency because of the uniform distribution of efficient active sites on the 3D hollow nanoarchitecture. These results were achieved by a chemical strategy for the design of the hierarchical hollow nanoarchitecture, providing the advantage of highly ordered nano/micro structures with hierarchical pores, furnishing maximum and multiple functionalities for a wide range of emerging applications.

## CONFLICT OF INTEREST

The authors declare no conflict of interest.

## ACKNOWLEDGEMENTS

This work was supported by the National Research Foundation of Korea (NRF) grant funded by the Ministry of Science, ICT, and Future Planning (Nos. 2016R1A2B2012728 and 2016M3A7B4909318) and by the Korea Research Institute of Chemical Technology (KRICT cooperation project).

## PUBLISHER'S NOTE

Springer Nature remains neutral with regard to jurisdictional claims in published maps and institutional affiliations.

1 Shim, H.-W., Park, S., Song, H. J., Kim, J.-C., Jang, E., Hong, K. S., Kim, T. D. & Kim, D.-W. Biomineralized multifunctional magnetite/carbon microspheres for applications in Li-ion Batteries and water treatment. *Chem. Eur. J.* **21**, 4655–4663 (2015).
2 Lee, G.-H., Park, J.-G., Sung, Y.-M., Chung, K. Y., Cho, W. I. & Kim, D.-W. Enhanced cycling performance of an $Fe^0$/$Fe_3O_4$ nanocomposite electrode for lithium-ion batteries. *Nanotechnology* **20**, 295205 (2009).
3 Ling, D., Lee, N. & Hyeon, T. Chemical synthesis and assembly of uniformly sized iron oxide nanoparticles for medical applications. *Acc. Chem. Res.* **48**, 1276–1285 (2015).
4 Tilley, S. D., Cornuz, M., Sivula, K. & Gratzel, M. Light-induced water splitting with hematite: improved nanostructure and iridium oxide catalysis. *Angew. Chem.* **122**, 6549–6552 (2010).
5 Cesar, I., Kay, A., Martinez, J. A. G. & Gratzel, M. Translucent thin film $Fe_2O_3$ photoanodes for efficient water splitting by sunlight: nanostructure-directing effect of Si-doping. *J. Am. Chem. Soc.* **128**, 4582–4583 (2006).
6 Cornell, R. M. & Schwertmann, U. *The iron oxides: structure, properties, reactions, occurrence and uses* (Wiley-VCH, Weinheim: Germany, 2003).
7 Santos-Carballal, D., Roldan, A., Grau-Crespo, R. & Leeuw, N. H. A DFT study of the structures, stabilities and redox behaviour of the major surfaces of magnetite $Fe_3O_4$. *Phys. Chem. Chem. Phys.* **16**, 21082–21097 (2014).
8 Parkinson, G. S., Novotny, Z., Jacobson, P., Schmid, M. & Diebold, U. Room temperature water splitting at the surface of magnetite. *J. Am. Chem. Soc.* **133**, 12650–12655 (2011).
9 Wang, P. & Lo, Irene M.C. Synthesis of mesoporous magnetic γ-$Fe_2O_3$ and its application to Cr(VI) removal from contaminated water. *Water Res.* **43**, 3727–3734 (2009).
10 Nassar, N. N. Kinetics, equilibrium and thermodynamic studies on the adsorptive removal of nickel, cadmium and cobalt from wastewater by superparamagnetic iron oxide nanoadsorbents. *Can. J. Chem. Eng.* **90**, 1231–1238 (2012).
11 Yadanaparthi, S. K. R., Graybill, D. & von Wandruszka, R. Adsorbents for the removal of arsenic, cadmium, and lead from contaminated waters. *J. Hazard. Mater.* **171**, 1–15 (2009).
12 Prasad, R., Pandey, R. & Barman, I. Engineering tailored nanoparticles with microbes: *quo vadis*? *WIREs Nanomed. Nanobiotechnol.* **8**, 316–330 (2016).
13 Fei, X., Li, W., Shao, Z., Seeger, S., Zhao, D. & Chen, X. Protein biomineralized nanoporous inorganic mesocrystals with tunable hierarchical nanostructures. *J. Am. Chem. Soc.* **136**, 15781–15786 (2014).
14 Wang, B., Chen, J. S., Wu, H. B., Wang, Z. & Lou, X. W. Quasiemulsion-templated formation of α-$Fe_2O_3$ hollow spheres with enhanced lithium storage properties. *J. Am. Chem. Soc.* **133**, 17146–17148 (2011).
15 Lou, X. W., Archer, L. A. & Yang, Z. Hollow micro-/nanostructures: synthesis and applications. *Adv. Mater.* **20**, 3987–4019 (2008).
16 Ma, F.-X., Hu, H., Wu, H. B., Xu, C.-Y., Xu, Z., Zhen, L. & Lou, X. W. (D. Formation of uniform $Fe_3O_4$ hollow spheres organized by ultrathin nanosheets and their excellent lithium storage properties. *Adv. Mater.* **27**, 4097–4101 (2015).
17 Wang, B., Wu, H., Yu, L., Xu, R., Lim, T.-T. & Lou, X. W. Template-free formation of uniform urchin-like α-FeOOH hollow spheres with superior capability for water treatment. *Adv. Mater.* **24**, 1111–1116 (2012).
18 Xu, J.-J., Xu, D., Wang, Z.-L., Wang, H.-G., Zhang, L.-L. & Zhang, X.-B. Synthesis of perovskite-based porous $La_{0.75}Sr_{0.25}MnO_3$ nanotubes as a highly efficient electrocatalyst for rechargeable lithium–oxygen batteries. *Angew. Chem. Int. Ed.* **52**, 3887–3890 (2013).
19 Cao, S.-W. & Zhu, Y.-J. Hierarchically nanostructured α-$Fe_2O_3$ hollow spheres: preparation, growth mechanism, photocatalytic property, and application in water treatment. *J. Phys. Chem. C* **112**, 6253–6257 (2008).

20 Koo, B., Xiong, H., Slater, M. D., Prakapenka, V. B., Balasubramanian, M., Podsiadlo, P., Johnson, C. S., Rajh, T. & Shevchenko, E. V. Hollow iron oxide nanoparticles for application in lithium ion batteries. *Nano Lett.* **12**, 2429–2435 (2012).
21 Zhang, J., Luan, Y., Lyu, Z., Wang, L., Xu, L., Yuan, K., Pan, F., Lai, M., Liu, Z. & Chen, W. Synthesis of hierarchical porous δ-$MnO_2$ nanoboxes as an efficient catalyst for rechargeable Li-$O_2$ batteries. *Nanoscale* **7**, 14881–14888 (2015).
22 Cheng, C., Shao, Z. & Vollrath, F. Silk fibroin-regulated crystallization of calcium carbonate. *Adv. Funct. Mater.* **18**, 2172–2179 (2008).
23 Shen, Y., Johnson, M. A. & Martin, D. C. Microstructural characterization of *Bombyx mori* silk fibers. *Macromolecules* **31**, 8857–8864 (1998).
24 Jin, H.-J. & Kaplan, D. L. Mechanism of silk processing in insects and spiders. *Nature* **424**, 1057–1061 (2003).
25 Nguyen, A. T., Huang, Q.-L., Yang, Z., Lin, N., Xu, G. & Liu, X. Y. Crystal networks in silk fibrous materials: from hierarchical structure to ultra performance. *Small* **11**, 1039–1054 (2015).
26 Löwen, H. Colloidal soft matter under external control. *J. Phys. Condens. Matter* **13**, R415–R432 (2001).
27 Ochi, A., Hossain, K. S., Magoshi, J. & Nemoto, N. Rheology and dynamic light scattering of silk fibroin solution extracted from the middle division of *Bombyx mori* silkworm. *Biomacromolecules* **3**, 1187–1196 (2002).
28 Zhang, C., Zhao, S., Jin, C., Koh, A. L., Zhou, Y., Xu, W., Li, Q., Xiong, Q., Peng, H. & Liu, Z. Direct growth of large-area graphene and boron nitride heterostructures by a co-segregation method. *Nat. Commun.* **6**, 6519 (2015).
29 Park, J. E., Lee, G.-H., Choi, M., Dar, M. A., Shim, H.-W. & Kim, D.-W. Comparison of catalytic performance of different types of graphene in Li-$O_2$ batteries. *J. Alloy. Compd.* **647**, 231–237 (2015).
30 Lee, J.-H., Black, R., Popov, G., Pomerantseva, E., Nan, F., Botton, G. A. & Nazar, L. F. The role of vacancies and defects in $Na_{0.44}MnO_2$ nanowire catalysts for lithium–oxygen batteries. *Energy Environ. Sci.* **5**, 9558–9565 (2012).
31 Lee, G.-H., Lee, S., Kim, J.-C., Kim, D. W., Kang, Y. & Kim, D.-W. $MnMoO_4$ electrocatalysts for superior long-life and high-rate lithium-oxygen batteries. *Adv. Energy Mater.* **7**, 1601741 (2016).
32 Song, K., Jung, J., Heo, Y.-U., Leze, Y. C., Cho, K. & Kang, Y.-M. α-$MnO_2$ nanowire catalysts with ultra-high capacity and extremely low overpotential in lithium–air batteries through tailored surface arrangement. *Phys. Chem. Chem. Phys.* **15**, 20075–20079 (2013).
33 Gao, R., Liu, L., Hu, Z., Zhang, P., Cao, X., Wang, B. & Liu, X. The role of oxygen vacancies in improving the performance of CoO as a bifunctional cathode catalyst for rechargeable Li-$O_2$ batteries. *J. Mater. Chem. A* **3**, 17598–17605 (2015).
34 Banger, K. K., Yamashita, Y., Mori, K., Peterson, R. L., Leedham, T., Rickard, J. & Sirringhaus, H. Low-temperature, high-performance solution-processed metal oxide thin-film transistors formed by a 'sol–gel on chip' process. *Nat. mater.* **10**, 45–50 (2011).
35 Bruce, P. G., Freunberger, S. A., Hardwick, L. J. & Tarascon, J.-M. Li-$O_2$ and Li-S batteries with high energy storage. *Nat. mater.* **11**, 19–29 (2012).
36 Ding, J., Li, B., Liu, Y., Yan, X., Zeng, S., Zhang, X., Hou, L., Cai, Q. & Zhang, J. Fabrication of $Fe_3O_4$@reduced graphene oxide composite via novel colloid electrostatic self-assembly process for removal of contaminants from water. *J. Mater. Chem. A* **3**, 832–839 (2015).
37 Nassar, N. N. Kinetics, mechanistic, equilibrium, and thermodynamic studies on the adsorption of acid red dye from wastewater by γ-$Fe_2O_3$ nanoadsorbents. *Sep. Sci. Technol.* **45**, 1092–1103 (2010).
38 Ho, Y. S. & McKay, G. Pseudo-second order model for sorption processes. *Process Biochem.* **34**, 451–465 (1999).
39 Chen, W., Duan, L., Wang, L. & Zhu, D. Adsorption of hydroxyl- and amino-substituted aromatics to carbon nanotubes. *Environ. Sci. Technol.* **42**, 6862–6868 (2008).
40 Hunter, C. A. & Sanders, J. K. M. The Nature of π–π interactions. *J. Am. Chem. Soc.* **112**, 5525–5534 (1990).



Supplementary Information accompanies the paper on the NPG Asia Materials website (http://www.nature.com/am)